MAX-PLANCK-INSTITUT FÜR PLASMAPHYSIK

GARCHING BEI MÜNCHEN

SCATTERING OF RARE GAS IONS FROM
METAL SURFACES

STREUUNG VON EDELGASIONEN AN
METALLOBERFLÄCHEN

W. Eckstein, H. G. Schäffler, H. Verbeek

IPP 9/16   January 1974

IPP 9/16   W. Eckstein   Scattering of Rare Gas

             H. G. Schäffler   Ions from Metal Surfaces

             H. Verbeek

                                  January 1974   (in English)

ABSTRACT
_____

The scattering of rare gas ions from polycrystalline and single crystal
metal targets is studied in the energy range of 2 to 16 keV. This report
deals with three aspects of ion scattering: 1. Noble gas ion scattering
as an analytical tool for surface analysis, 2. The inelastic energy losses
in the scattering processes, and 3. The influence of the crystal structure
on the scattering. The last part contains some model calculations to
explain the experimental results.

Die Streuung von Edelgasionen an poly- und einkristallinen Metall Targets
wurde im Energiebereich von 2 bis 16 keV untersucht. Dieser Bericht
handelt von drei Aspekten der Ionenstreuung: 1. Die Edelgasstreuung
als Mittel zur Oberflächenanalyse, 2. Die inelastischen Energieverluste
bei der Streuung und 3. Der Einfluß der Kristallstruktur auf die Streu-
ung. Der letzte Teil enthält einige Modellrechnungen, die zum Verständnis
der Experimente angestellt wurden.

1. INTRODUCTION

The scattering of rare gas ions from metal surfaces has been the subject of investigations in various laboratories for a number of years. The comprehensive literature is discussed in detail by Mashkova and Molchanov in a recently published review article /1/. The present paper therefore only makes reference to a few special studies.

Our investigations with rare gas ions were conducted parallel to measurements of the backscattering of hydrogen ions /2,3/ and were likewise done with the BOMBARDON apparatus, which has already been described in detail /4/. In this device targets can be bombarded with ion beams of 2 - 20 keV. The target is placed in a UHV chamber, where it is mounted on a goniometer head, on which it can be rotated about three mutually perpendicular axes. The backscattered ions are analyzed with an electrostatic energy spectrometer which can be swept about the target and are detected with a multiplier.

In this report three aspects of rare gas ion scattering from metal surfaces are discussed on the basis of experimental results and model calculations:

- Scattering as a method of analysis
- Inelastic energy losses due to scattering
- Influence of crystal structure on scattering.

2. SCATTERING OF RARE GAS IONS AS A METHOD OF ANALYSIS

In many cases rare gas ions are scattered from the individual surface atoms of the solid. The energy loss due to the scattering and the scattering angle are then related by the purely kinematic formula:

$$\frac{E_1}{E_0} = f(A, \vartheta)$$

$$f(A, \vartheta) = \frac{1}{(1+A)^2} \left\{ \cos \vartheta \pm \left[A^2 - \sin^2 \vartheta \right]^{1/2} \right\}^2 \qquad (1)$$

where the notations are as follows:

E_o - energy of ions before collision

E_1 - energy of ions after collision

ϑ - scattering angle in laboratory system

M_1 - mass of colliding particle

M_2 - mass of target atoms

$A = \dfrac{M_2}{M_1}$

By determining the energy of the particles after collision for a fixed scattering angle it is possible to obtain the mass M_2 of the scattering atom. This affords a method of surface analysis. This technique was first used by D. P. Smith /5/ and later elaborated by Ball et al. /6/, Goff /7/, and Heiland and Taglauer /8/.

Given the energy resolution $E/\Delta E$ of the spectrometer used, it is possible to calculate the attainable mass resolution:

$$\frac{M_2}{\Delta M_2} = g(A, \vartheta) \frac{E}{\Delta E} \tag{2}$$

$$g(A, \vartheta) = \frac{2A}{A+1} \cdot \frac{A + \sin^2\vartheta - \cos\vartheta\sqrt{A^2 - \sin^2\vartheta}}{A^2 - \sin^2\vartheta + \cos\vartheta\sqrt{A^2 - \sin^2\vartheta}} \qquad \text{for} \quad A > 1$$

Figure 1 shows the dependence of the function g on the mass ratio A for two scattering angles, and Fig. 2 the dependence on the scattering angle ϑ. The curves show that the mass resolution is most favourable for small A and large ϑ. The mass resolution is limited, however, by the smallest detectable scattering intensity.

The scattering cross-section, and hence the intensity, decreases as the scattering angle becomes larger. This is shown in Fig. 3, where the scattering cross-section is plotted as a function of the scattering angle for 15.1 and 4.8 keV Ne → Ni according to the tables of Robinson /9/. The cross-section does become larger with increasing A for a certain ion mass M_1, but at the same time the mass resolution undergoes a corresponding decrease (Fig. 2).

When an electrostatic spectrometer is used, the recorded scattering inten-
sity decreases with decreasing energy because the energy interval is
$\Delta E \propto E$. The detection probability is therefore low for small A and large ϑ
since the energy of the backscattered ions is small.

It should also be noted that it is only for $A > 1$ that all masses can be de-
tected at all scattering angles. For $A < 1$ scattering only occurs at angles
for which $\sin^2\vartheta < A^2$.

An experimental example is given in Fig. 4, which shows the energy spectra
of Ne^+ ions backscattered from a Ni target. The increase in resolution and
decrease in intensity as the scattering angle becomes larger are obvious.
At $\vartheta = 120^\circ$ and $\vartheta = 150^\circ$ the two Ni isotopes with masses 58 and 60 can be
separated without trouble. In this case the value for A and $E/\Delta E$ were
$A = 2.9$ and $E/\Delta E = 140$. The small peaks occurring at half the energy of
the large maxima can be ascribed to Ne^{++} ions. In the spectra the Ni^{62}
isotope (3.7% in the natural isotope mixture) can just be recognized. The
detection limit in this case is thus in the region of a few per cent.

Another example showing the detection of oxygen on a vanadium surface is
given in Fig. 5. The upper spectrum was recorded after the target had
been heated for a few minutes to about $750^\circ C$. This causes oxygen to diffuse
to the surface, and this can be detected as a maximum in the spectrum.
After a certain bombardment dose the oxygen is sputtered and the oxygen
maximum vanishes. At the same time a small maximum (denoted by "V^+"
appears which can be ascribed to vanadium "sputtered" in a binary collision.
Besides presenting ion scattering as a method of analysis, Fig. 5 also
demonstrates a certain disadvantage, namely that the surface can be changed
relatively fast by the measurement if the bombardment dose required for
analysis is not kept as low as possible. In this case the oxygen maximum
vanishes after a bombardment dose of approximately $1,5 \cdot 10^{-2}$ Cb/cm^2,
while about $2 \cdot 10^{-3}$ Cb/cm^2 was needed to record the spectrum.

The backscattering spectra here have a somewhat different shape to those
at lower energies (< 1200 eV) as was investigated by Heiland and Taglauer
/8/, /18/. Particularly at small scattering angles there is an appreciable

scattering intensity at energies below the binary collision maximum (see also Figs. 6, 11 and 17). This is due to ions which are scattered deeper inside the solid. At low energies the backscattering maxima are approximately symmetric because only the ions backscattered from the surface have a chance of not being neutralized. Heiland et al. /18/ find the maximum of the target atoms "sputtered" in binary collisions to be at $E_o < 1200$ eV only when bombardment is with Ar^+ ions. They, too, observed an appreciable change of the surface during the measurements.

3. INELASTIC ENERGY LOSSES DUE TO SCATTERING

The energies of the ions elastically backscattered from the surface atoms in binary collisions are given by formula (1). It is experimentally observed, however, that the corresponding maxima are shifted towards lower energies. In Figs. 4, 5 and 6 the energies calculated with formula (1) are denoted by arrows. (In Figs. 5 and 6 at $\vartheta = 30^o$ the maximum is broadened by multiple scattering). The shift of the maxima is distinctly larger than the experimental errors. It was possible to determine the energy exactly to within ± 25 eV and to set the scattering angle exactly to within $\pm 0.3^o$. The observed shifts would require deviations of the scattering angles from the nominal value of several degrees. It must therefore be assumed that the inelastic energy losses due to scattering cannot be neglected. Figure 7 shows the inelastic energy loss due to scattering of Ne^+ ions from Ni as a function of the scattering angle. In Fig. 8 and Fig. 9 the inelastic energy losses are depicted as functions of the primary energy E_o and the energy E_1 after the collision respectively.

In our energy range the estimate by Firsov /10/ for the electronic energy loss should be valid. This would make the inelastic energy loss

$$\Delta E_{th} = \frac{(Z_1 + Z_2)^{5/3} \cdot 4.3 \cdot 10^{-8} u}{[1 + 3.1 (Z_1 + Z_2)^{1/3} \cdot 10^7 R_o]^5} \,, \tag{3}$$

where Z_1 and Z_2 are the atomic numbers of the collision partners, u the velocity of the incoming particle (if the other particle is at rest), and R_o the distance of closest approach, which is a function of the primary energy E_o and the scattering angle ϑ. The R_o values can be interpolated from the tables of Robinson (9) and were used to calculate the energy losses according to equation (3). A comparison between the experimental results and the Firsov theory is shown in Fig. 10, where the ratio of the experimental to the theoretical values are shown as function of E_1/E_o. As one expects the agreement is satisfactory only for small elastic energy losses i.e. when E_1 is not very different from E_o. The theoretical values calculated with $u = v_o$ are too large in most cases but to small if calculated with $u = v_1$ (velocity of the scattered ion).

As the scattering angles decrease there is more probability not only of purely binary collisions but also of the multiple scattering processes described in the following section. These produce the "shoulders" on the high-energy side of the maxima in Fig. 6. At smaller scattering angles the shoulders cause the binary collision maximum to be shifted to higher energies. The measured energy losses for smaller scattering angles are therefore probably still too small.

4.   INFLUENCE OF CRYSTAL STRUCTURE ON SCATTERING

The maxima in Figs. 4, 5 and 6 ascribed to binary collisions with surface atoms according to formula (1) show more or less pronounced shoulders on the high-energy sides. These can be explained in terms of several successive binary collisions (multiple collisions) /11, 12, 13, 14/. This effect is best investigated by means of scattering from single crystal surfaces. Figure 11 shows the backscattering spectra of 10 keV Ne^+ ions impinging at an angle of $\psi = 20^o$ at a $\langle 110 \rangle$ chain in the (100) surface of a vanadium single crystal. At some scattering angles two distinct maxima can be observed. The presence of two maxima at a fixed scattering angle can be explained in terms of multiple scattering from single chains /15, 16, 17, 18, 19/. Model calculations were made by computer to clarify the effects of multiple scattering. The results are discussed below.

4.1 COMPUTER CALCULATIONS

The scattering of particles from an atomic chain is simulated according to the following scheme. An ion with energy E_o impinges at an angle ψ on a rigid one-dimensional chain of atoms, collides in succession with the individual atoms and leaves the chain again with a total scattering angle ϑ and an energy E_1. The first impact parameter p_1 is chosen such that the corresponding angle of deflection is smaller than 0.01^o. The collision parameter for the next collision with the next chain atom at a distance d is found from Fig. 12 (according to Parilis [11]) to be

$$p_2 = p_1 - d \sin (\psi - \vartheta_1) \tag{4}$$

and the collision parameters for the subsequent collisions are similarly determined. For every collision the corresponding scattering angle is determined from the collision parameter and the corresponding energy by means of Lindhard's magic formula [20] and Molière's interaction potential [21].[+)] The elastic energy loss is taken into account by subtracting after every collision the transmitted energy corresponding to the scattering angle from the energy of the scattered ion. The ion keeps colliding with chain atoms until the angle of deflection is smaller than 0.01^o. An ion beam is simulated by using this method to calculate a series of ion paths with successively larger first collision parameter until the first ion path (shifted by one atomic spacing) is again obtained, i.e. when p_2 becomes equal to the p_1 of the first ion path.

An example is discussed on the basis of Figs. 13, 14 and 15. Ne^{20} ions with 8 keV impinge at an angle of $\psi = 15^o$ on a $\langle 110 \rangle$ chain of a Ni^{58} crystal and are scattered from this chain. In the lower part of Fig. 13 the possible energies of the scattered ions are plotted with a dashed line as a function of the total scattering angle. In this case, only a scattering angle range of 26.7^o to 85.8^o is possible. For a fixed scattering angle in this range two energies

---

[+)] The potential is of the form

$$V(r) = \frac{Z_1 Z_2}{r} e^2 \phi(r/a) \quad \text{with} \quad \phi(r/a) = 0.1\, e^{-6\, r/a} + 0.55\, e^{-1.2\, r/a} + 0.35\, e^{-0.3\, r/a}$$

and $\quad a = 0.8853\, a_o\, (Z_1^{2/3} + Z_2^{2/3})^{-\frac{1}{2}}$.

are possible. All possible energies lie on a closed loop located above the (solid) binary collision curve according to formula (1).

The generation of a loop is a shadowing effect. When an ion impinges on a chain at a sufficiently acute angle, small collision parameters and hence large scattering angles become impossible (see Fig. 10). For the same reason there can be no arbitrarily small total angles of deflection because the ions departing at small angles to the chain are then scattered by the following ions at larger angles. The extent of the loop, i.e. the possible scattering angle range, depends on the angle of incidence ψ, the energy E_o of the incident ion, the atomic spacing d in the chain, and the atomic numbers Z_i (i.e. interaction potential) of the ions and atoms. As ψ, d or E_o becomes smaller or Z_i becomes larger, the shadowing effect increases and the loop becomes smaller. If the angle of incidence ψ is further reduced, the loop contracts to a point so that the angles of incidence and emergence become equal. The ions are then reflected from the chain; the transverse energy is conserved. If ψ is increased, an angle of incidence is generated for which the loop is no longer closed at large angles. Further increases of ψ cause the scattering intensity in the high-energy branch to decrease fast and the low-energy branch approaches the binary collision curve. Multiple scattering is then only of minor importance.

The two energies belonging to one ϑ can be roughly estimated by combining the individual angles of deflection. The bottom branch of the loop (Fig. 13 bottom, dashed)is characterized by the fact that the scattering from the chain is mainly governed by one large angle of deflection. The top branch (dot-dashed) is characterized by the fact that two collisions make an essential contribution to the total deflection (see Fig. 14). This becomes more obvious at lower energies or higher atomic numbers.

The two types of symmetric scattering, for which the angles of incidence and emergence are equal, i.e. $\vartheta = 2\psi$, A (with even number of single collisions) and B (with odd number of single collisions) do not lead to special points on the loop in Fig. 13. At point C the loop comes closest to the binary collision curve. This point is characterized by the fact that, when the total

scattering angle is split into the largest individual scattering angle ϑ_{max} and the residual angle $\Delta\vartheta$, i.e. $\vartheta = \vartheta_{max} + \Delta\vartheta$, $\Delta\vartheta$ has a minimum. The contribution of the main scattering angle to the total scattering angle $\vartheta_{max}/\vartheta$ is plotted in the upper part of Fig. 13 for the high-energy (dot-dashed) and low-energy (dashed) branches of the loop. In the high-energy branch ϑ_{max} is always smaller than in the low-energy branch since it follows from formula (1) that

$$f(\vartheta_1 + \vartheta_2) \leq f(\vartheta_1) \cdot f(\vartheta_2) \quad .$$

The difference between the scattering processes leading to the high and low-energy branches of the loop are slight. This is seen in, for instance, the statistics of the individual scattering processes occurring (Fig. 14). In the low-energy branch the angle range 5° to 20° does not occur. On the other hand, the individual scattering angles above 20° and below 5° are much more frequent than in the high-energy branch. In Fig. 15 the size of the individual scattering angles ϑ_i is plotted as a function of the number of collisions preceding. The strongest deflection in both branches occurs at the fourth single collision (with the definition chosen for the first collision).

The intensity distribution along the loop is represented in Fig. 16. It was determined from the statistics of the calculated ion paths. The intensity in the low-energy branch is somewhat higher than in the high-energy branch. It is highest at the ends of the loop. When making a comparison with the experiment, however, allowance should be made for the fact that only the scattered ions can be detected. The neutralization probability can, however, be different for different branches of the loop.

4.2 COMPARISON OF THE EXPERIMENTAL RESULTS WITH COMPUTER CALCULATIONS

A few typical experimental backscattering spectra of 10 keV Ne^+ ions from a vanadium $\langle 110 \rangle$ chain are shown in Fig. 11. In many cases the two maxima for the doubly charged backscattered Ne^{++} ions are better separated than for Ne^+. An example is given in Fig. 17. In Figs. 18, 19 and 20 the energy values of the maxima as derived from the spectra were plotted versus

the scattering angle set. The solid curves represent the values calculated according to the model described in Section 4.1.

For the scattering angles at which two energies are predicted by the model two energies are also found experimentally. The existence of loops is thus confirmed. The spacing between the two maxima observed agrees very well with the theoretical width of the loops. (The narrow loop for $\psi = 10^o$ in Fig. 19 was not resolved experimentally). The starting point of the loops, i.e. the smallest possible scattering angle ϑ_{min} agrees well with the calculated value within the margins of error. Heiland et al. /18/, on the other hand, observed in a Ne^+ scattering experiment with a Ni target using energies below 1 keV a shift of the whole loop towards smaller scattering angles. The experimentally observed loops are appreciably shifted towards lower energies compared with those calculated. This can be explained in terms of inelastic energy losses, as in Sektion 3, which were not allowed for in the computer calculation, Furthermore, maxima in the backscattering spectra are also found outside the theoretically possible scattering angle range. These are then close to the theoretical binary collision curve. Their intensity, however, is much lower than would be expected from the increasing cross-section at small angles.

In the experiment the ions incident on the crystal surface are scattered not only from the isolated chains, as was assumed for the calculations. The majority of the ions rather impinge between the chains. Van Veen et al. /22/ have shown, however, that in a two-dimensional calculation loops quite similar to those due to scattering from isolated chains are obtained, there being an additional slight scattering intensity outside the loops. This contributes to the background in the backscattering spectra. Furthermore, no ideal chains are obtained in the experiment. If defects in the chains are assumed in the calculations, the calculations show that the scattering can occur for other combinations of energy and angle. This is discussed in the next section.

4.3 INFLUENCE OF LATTICE DEFECTS ON CHAIN SCATTERING

The following lattice defects were taken into account for the computer cal-
culations: a single atom is missing in a long chain("vacancy") a second super-
posed chain starts or terminates ("upward step" and "downward step"). The
result of such a calculation for bombardment of vanadium with Ne^+ ions along
a $\langle 110 \rangle$ chain is shown in Fig. 21. The loop due to scattering from the
ideal chain is reduced to a point (denoted by "chain" in Fig. 21) owing to the
small bombardment angle $\psi = 8^\circ$. To the left of this point scattering inten-
sity is obtained by downward steps, and to the right a new loop by upward
steps, the low-energy branch practically coinciding with the binary collision
curve. Within these loops scattering intensity is obtained on a new, narrow
loop by defects in the chains (denoted by "vacancy").

This thus explains why scattering intensity was found in Figs. 18,19 and 20
where it would not be expected after scattering from ideal chains. It is
difficult to decide, however, what kind of chain defects are the main cause
of the prohibited scattering intensity.

The energies of the target atoms sputtered in head-on-collisions (denoted
by "V^+ sputtered") are well below the binary collision curve. They are
therefore easy to detect experimentally with an energy analyzer alone. This
is no longer true when the incident ions have higher masses than the target
atoms. The calculation of Kr^+ scattering from copper $(M_1 > M_2)$ is repre-
sented in Fig. 22. Here the gas ions scattered from ideal and imperfect
chains intersect the curve of the "sputtered" target atoms several times.
Measured spectra are therefore hard to interpret if energy analysis is not
accompanied by mass analysis. On the other hand, the curves are far apart
as regards energy, and so they are easier to resolve experimentally. The
scattering of Kr^+ with sumaltanous energy and mass analyses was investigated
in detail by Begeman et al /23/. They do not, however, find any target ions
for $\vartheta = 30^\circ$ and various ψ , as would be expected from Fig. 22. This may
have various reasons. In Fig. 22 (and Fig. 21) there is no information on
the intensity with which certain combinations of energy and scattering angle
occur. Furthermore, the probability of the target ions being emitted in the
charged state becomes less than that of the bombardment ions.

Figure 23 shows a few experimental backscattering spectra of 8.22 keV Kr^+ from the $\langle 110 \rangle$ chains of vanadium. The energy of the target atom scattered in the binary collision is denoted be "$Kr^+ \rightarrow V$", that of the target atoms "sputtered" in the binary collision by "V^+". This figure shows how the shape of the backscattering spectra and their intensity already changes with relatively small changes of the angle of incidence ψ for a fixed scattering angle $\vartheta = 30^o$. To interpret these spectra, even more extensive computer calculations are required. It will then perhaps be possible, however, to decide from the backscattering spectra how strongly disturbed the surface of the investigated crystals is.

5. ACKNOWLEDGEMENTS

REFERENCES

/1/   E. S. Mashkova, V. A. Molchanov, Rad. Eff. **16**, 143 (1972)

/2/   W. Eckstein, H. Verbeek, J. Vac. Sci. Techn. **9**, 612 (1972)

/3/   W. Eckstein, H. G. Schäffler, H. Verbeek, Rad. Eff. **18**, 263 (1973)

/4/   W. Eckstein, H. Verbeek, Vacuum **23**, 159 (1973); Report IPP 9/7 (1972)

/5/   D. P. Smith, Surf. Sci. **25**, 171 (1971)

/6/   D. J. Ball, T. M. Buck, D. McNair, G. G. Weathy, Surf. Sci. **30**, 69 (1972)

/7/   R. F. Goff, J. Vac. Sci. Techn. **9**, 154 (1972) (Abstract)

/8/   W. Heiland, E. Taglauer, J. Vac. Sci. Techn. **9**, 620 (1972)

/9/   M. T. Robinson, Report ORNL - 4556 (1970)

/10/   O. B. Firsov, Sov. Phys. JETP **36** (9) 5 1076 (1959)

/11/   E. S. Parilis, Proc. VIIth Int. Conf. Phenomena, Ionized Gases, Belgrade, 1965 p. 129

/12/   E. S. Mashkova, V. A. Molchanov, Sov. Phys. Doklady **12**, 133 (1967)

/13/   V. M. Kivilis, E. S. Parilis, N. Yu. Turaev, Sov. Phys. Doklady **15**, 587 (1970)

/14/   I. N. Evdokimov, E. S. Mashkova, V. A. Molchanov, Sov. Phys. Doklady **14**, 467 (1969)

/15/   S. D. Marchenko, E. S. Parilis, N. Yu. Turaev, Sov. Phys. Doklady **17**, 877 (1973)

/16/   D. G. Armour, G. Carter, A. G. Smith, Rad. Eff. **3**, 175 (1970)

/17/   M. Aissa, E. S. Mashkova, V. A. Molchanov, Yu. G. Skripka, Sov. Phys. Solid State **12**, 1643 (1971)

/18a/ W. Heiland, H. G. Schäffler, E. Taglauer, Surf. Sci. **35**, 381 (1973)

/18b/ W. Heiland, E. Taglauer, Rad. Eff. **19**, 1 (1973)

/19/   E. S. Mashkova, V. A. Molchanov, Rad. Eff. **13**, 183 (1972)

/20/   J. Lindhard, V. Nielsen, M. Scharff, Mat. Fys. Medd. Dan. Vid. Selsk. **36**, No 10 (1968)

/21/   G. Moliere, Z. f. Naturforschg. **2a**, 133 (1947)

/22/   A. van Veen, J. Haak, Physics Lett. **40a**, 378 (1972)

/23/   S. H. A. Begemann, A. L. Boers, Surf. Sci. **30**, 134 (1972)
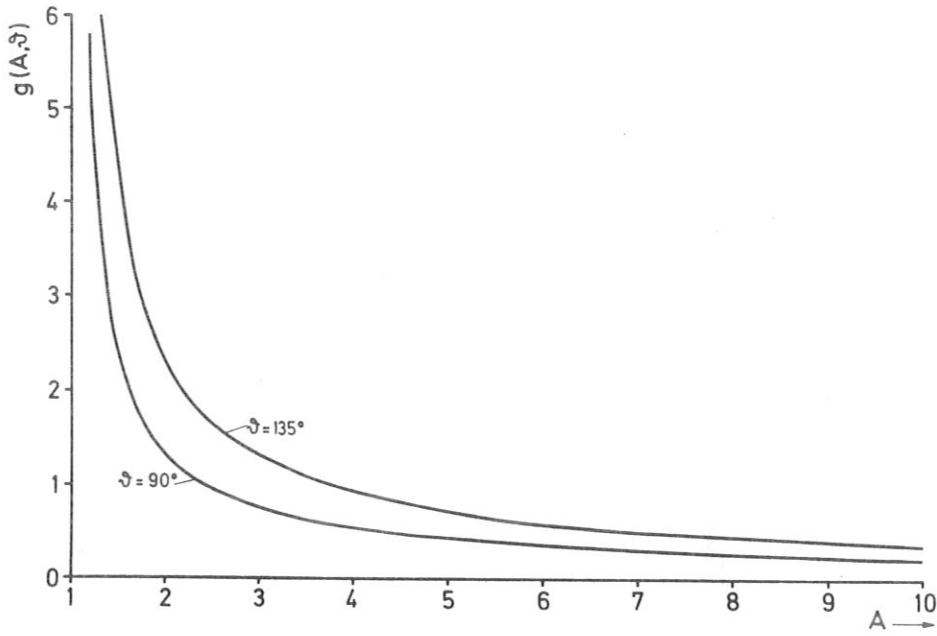
Fig. 1: The function g (A, ϑ) governing the mass resolution, versus A = M$_2$ for the scattering angles

$$\overline{M_1}$$

ϑ = 90° and ϑ = 135° (acc. to formula (2) on p.2).
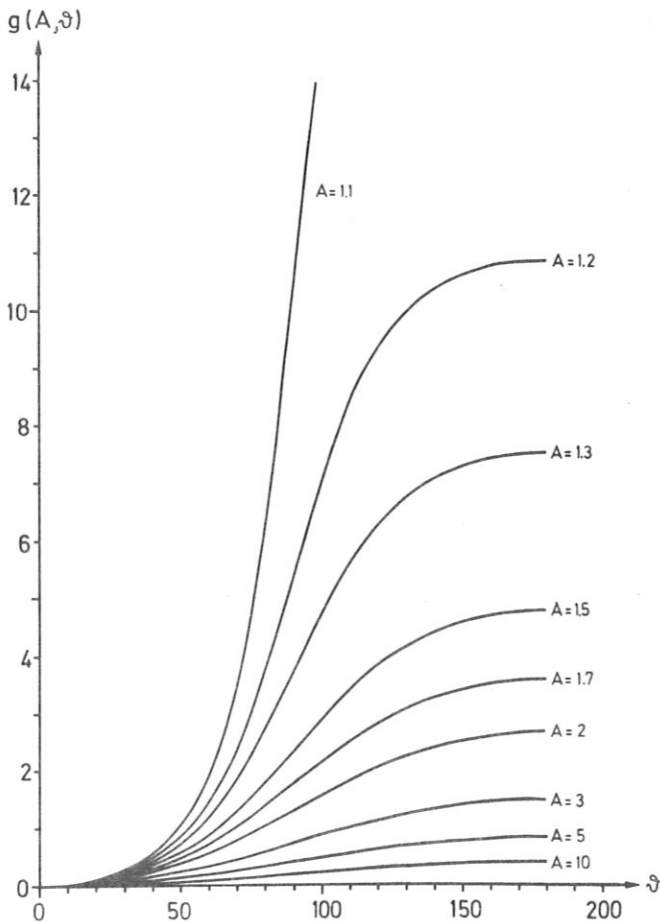
Fig. 2:

The function g (A, ϑ) governing the mass resolution, versus the scattering angle ϑ (acc. to formula (2) on p. 2).
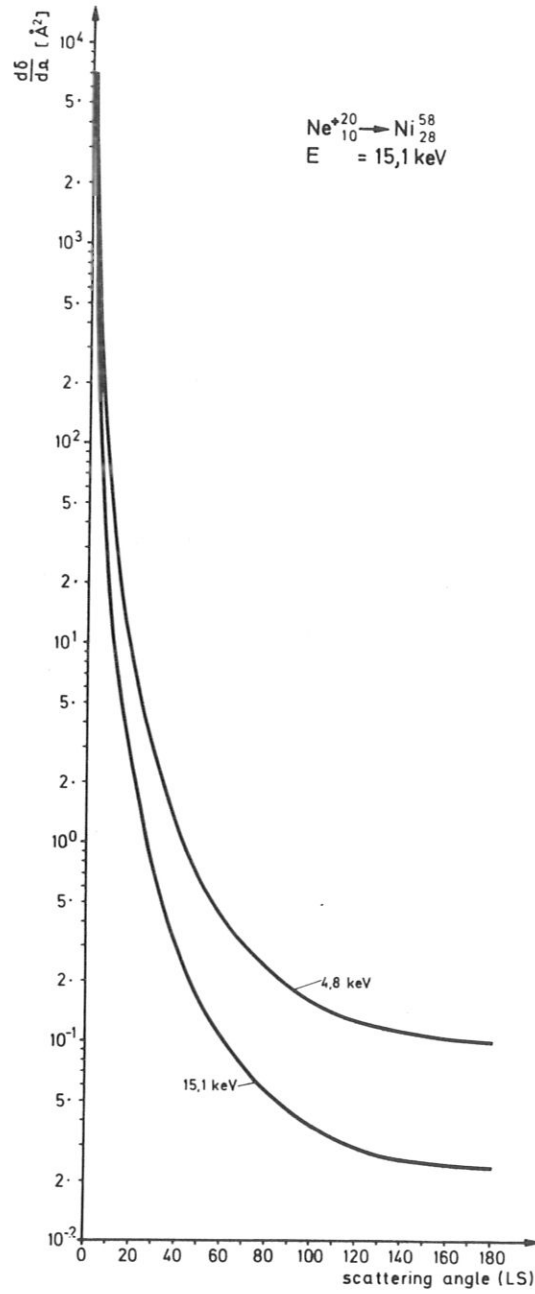
Fig. 3: Differential scattering cross-section
versus the scattering angle in the
laboratory system (acc. to M.T.Robinson (9)).
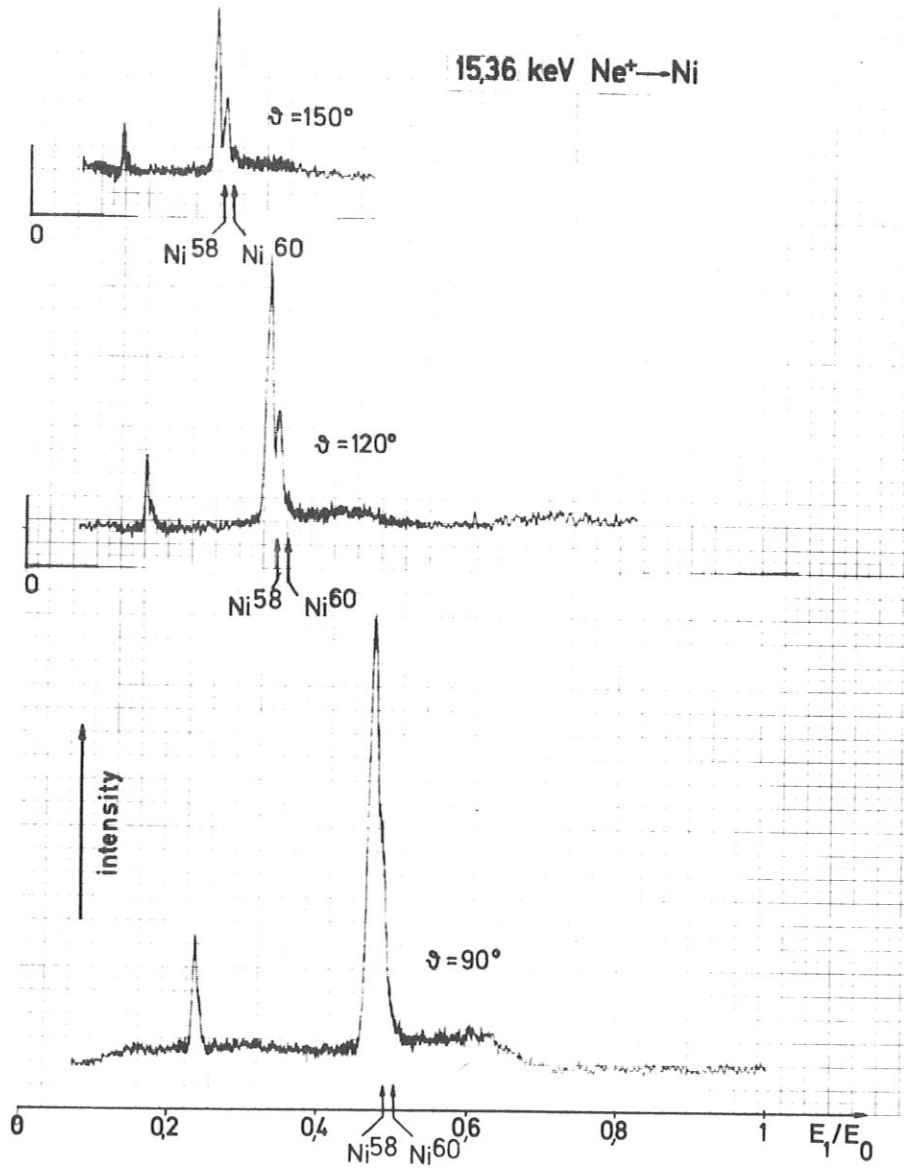
Fig. 4: Backscattering spectra of 15.36 keV
Ne$^+$ ions from Ni for the scattering
angles ϑ = 150°, 120° and 90°.
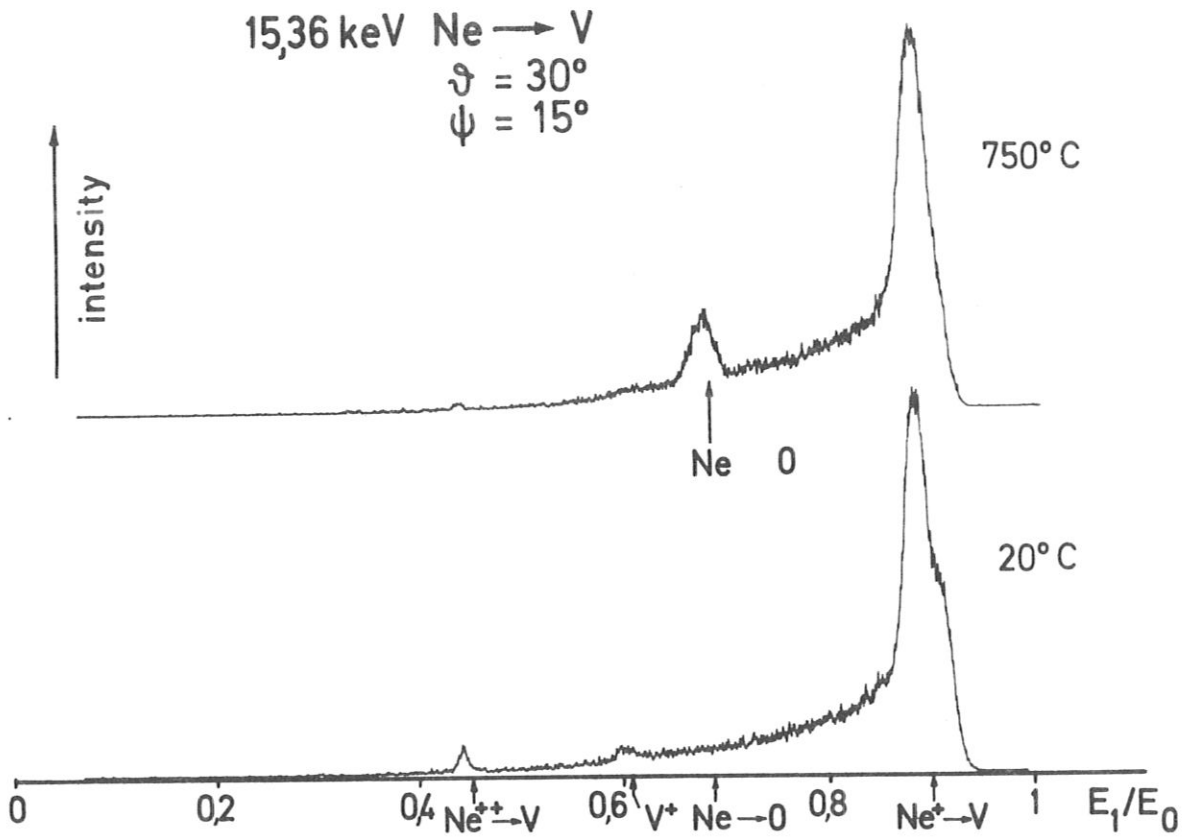
Fig. 5: Backscattering spectra of 15.36 keV Ne$^+$ ions from vanadium.
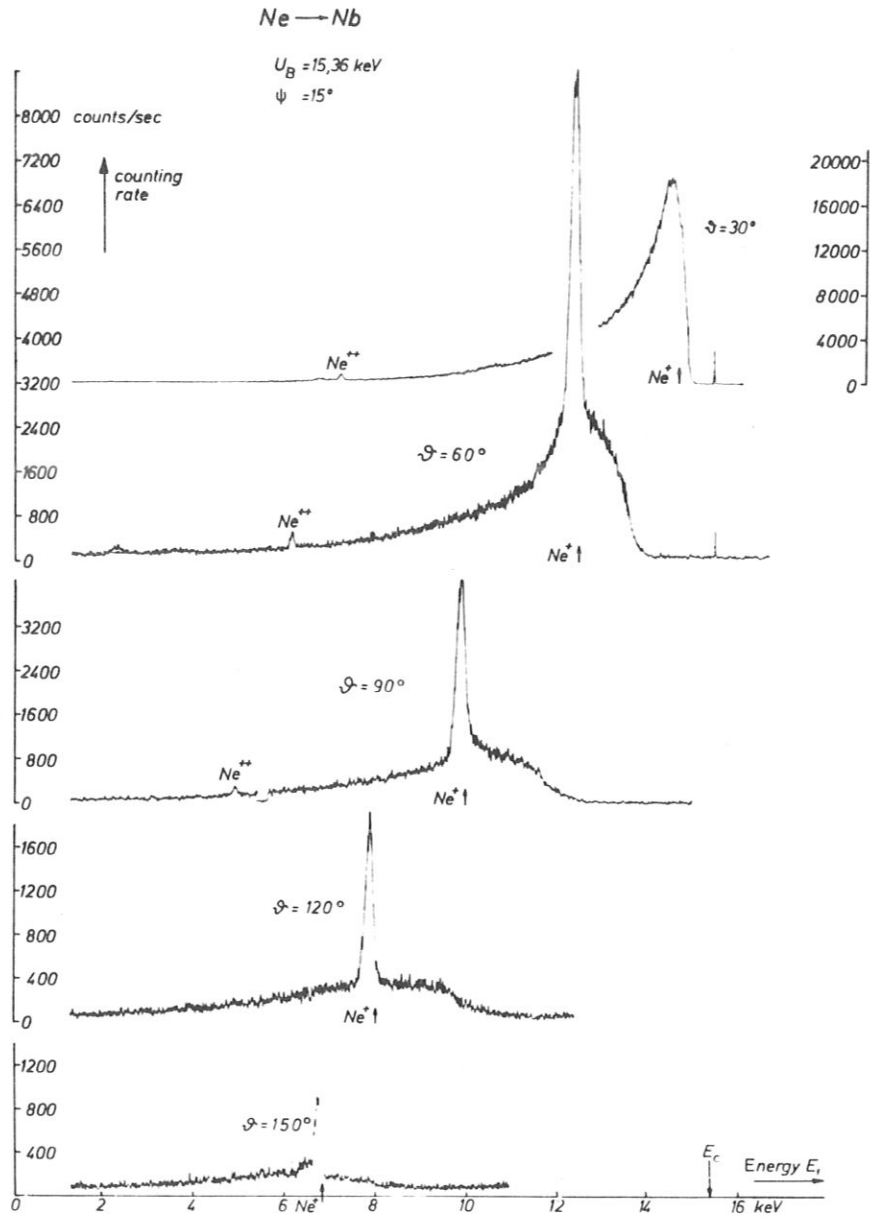
Fig. 6: Backscattering spectra of 15.36 keV Ne$^+$ ions from polycrystalline Nb for various scattering angles ϑ .
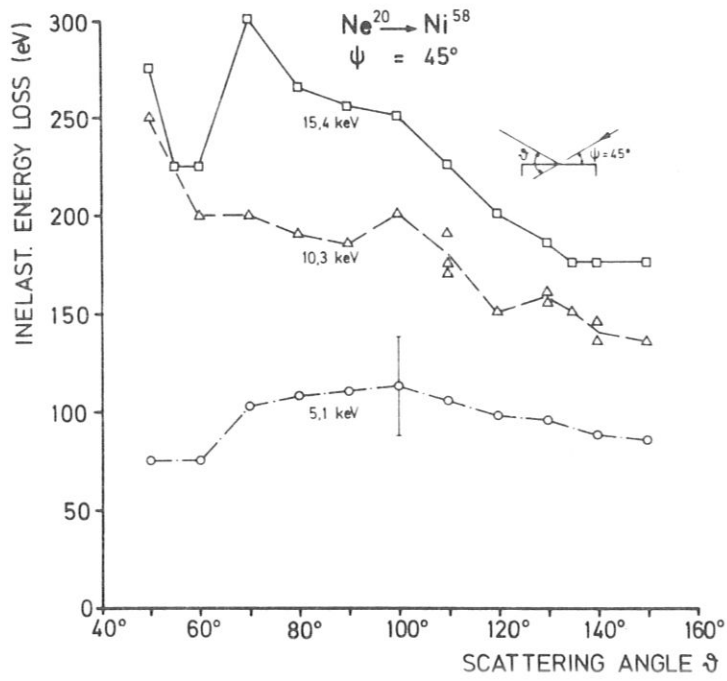
Fig. 7: Inelastic energy losses of Ne[+] ions scattered
from Ni, as a function of the scattering angle ϑ .
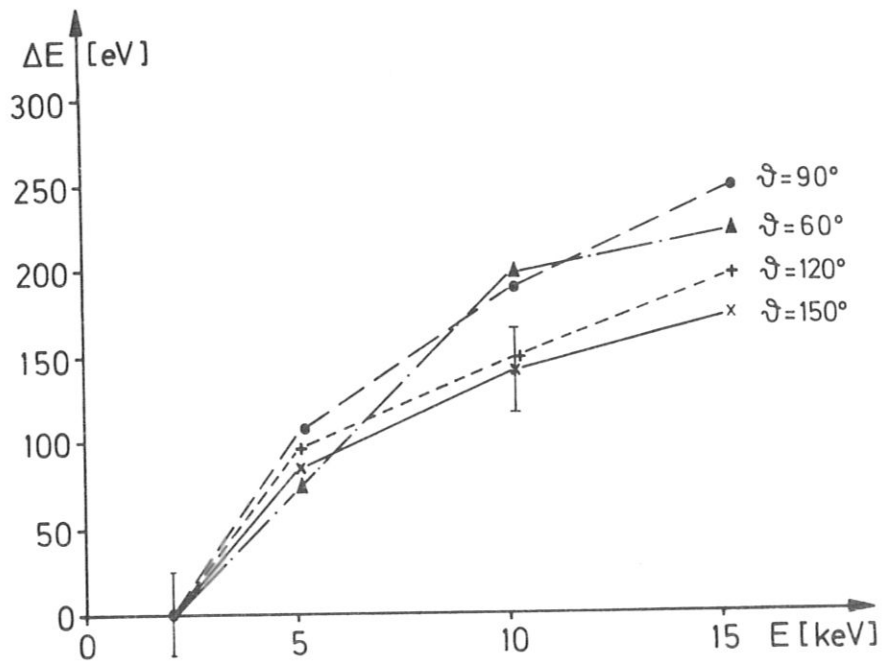
Fig. 8: Inelastic energy losses of Ne[+] ions scattered
from Ni, as a function of the primary energy E_o.
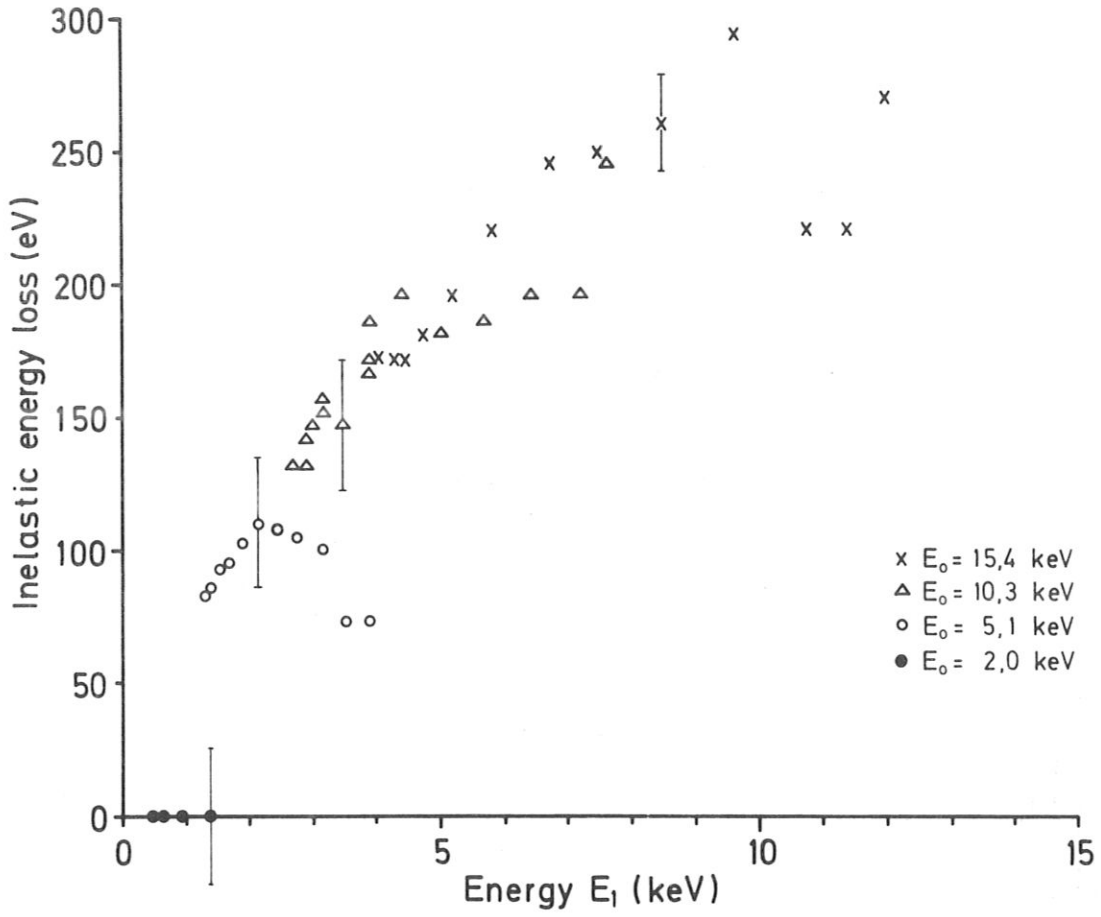
Fig. 9: Inelastic energy losses of Ne$^+$ ions scattered from Ni, as a function of their energy E_1 after scattering.
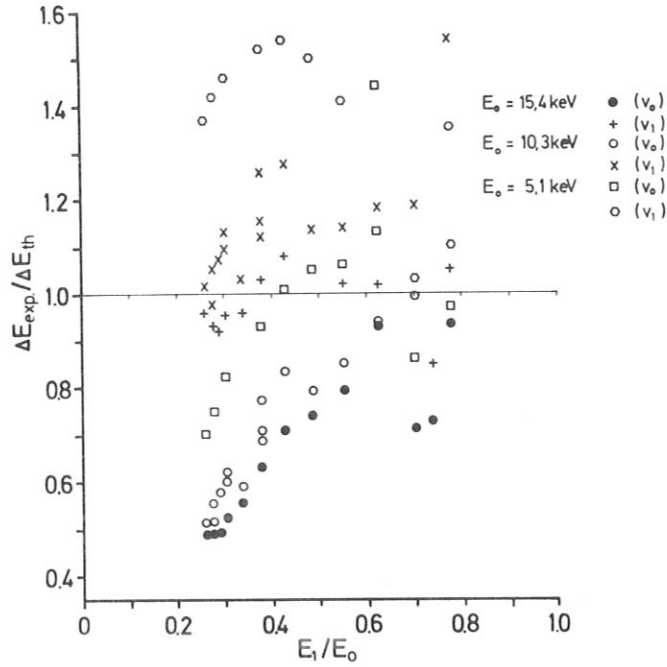
Fig. 10: Ratio of experimentally observed inelastic
energy losses and theoretical values accor-
ding to formula (3) page 4 as a function of
the energy after elastic collisions.
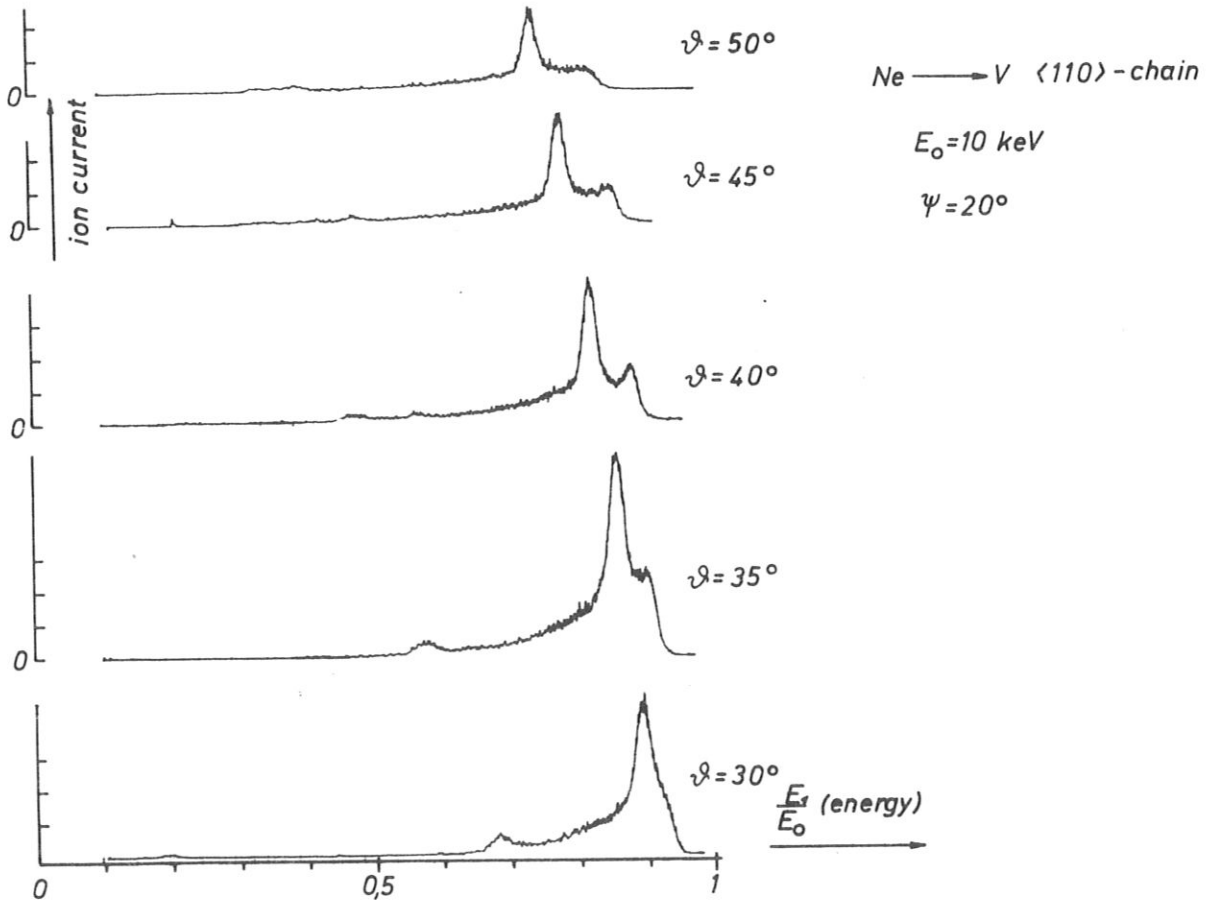
Fig. 11: Energy distributions of 10 keV Ne$^+$ ions scattered
from a $\langle 110 \rangle$ chain of vanadium.
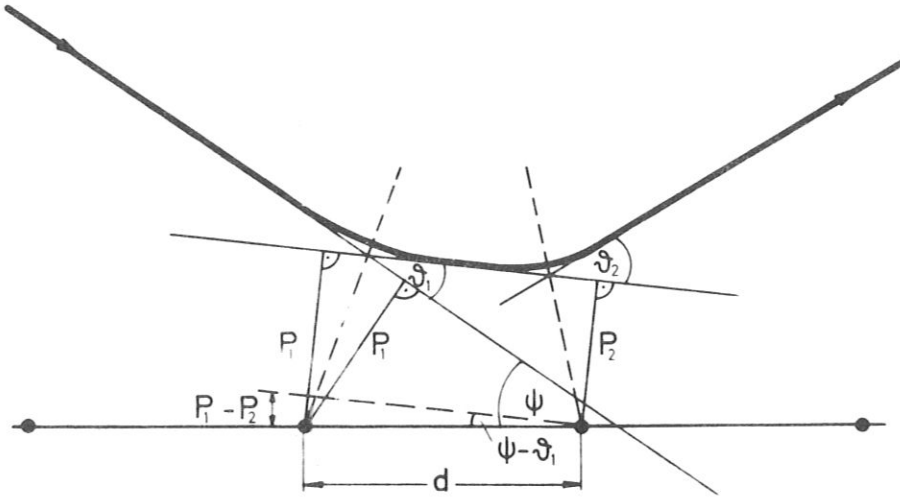
Fig. 12: Calculation of the impact parameters p in scattering from an atomic chain (acc. to Parilis /11/).
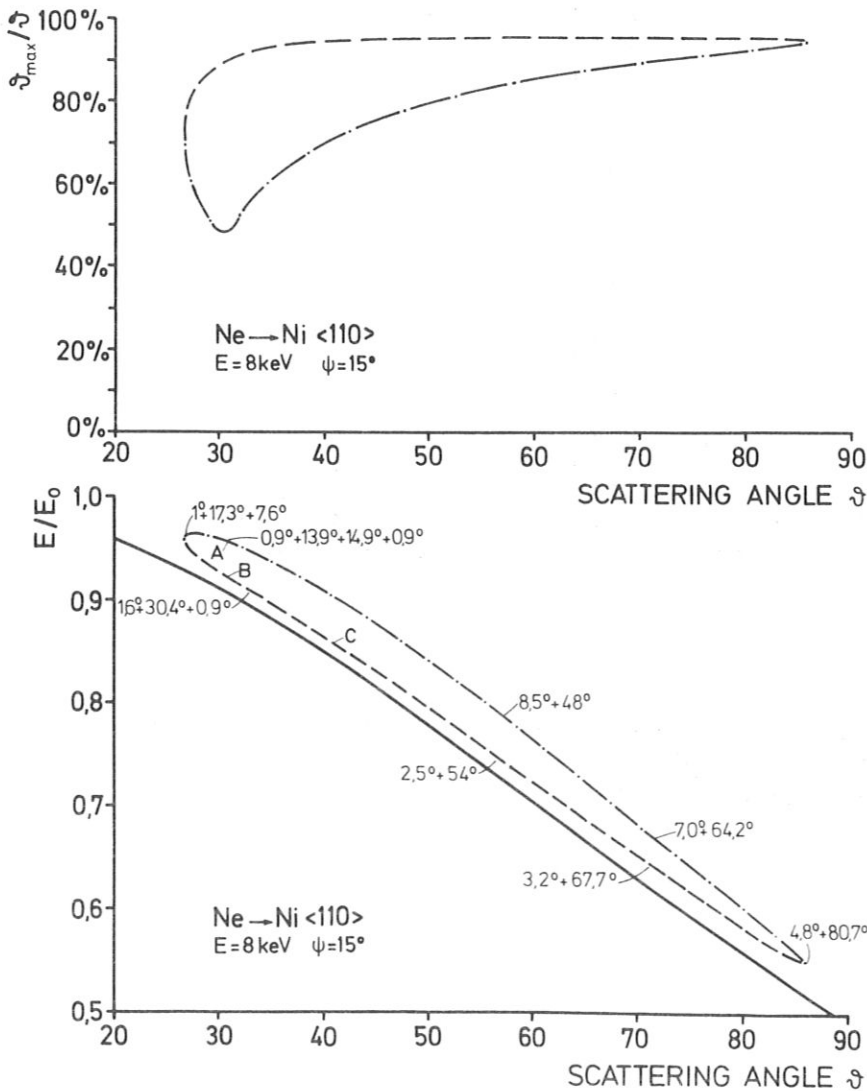
Fig. 13:

Bottom:

Possible energies of Ne⁺ ions scattered from an ideal ⟨110⟩ chain of Ni (dashed, dot-dashed curves). The solid line represents the binary collision curve acc. to formula (1) (for points A,B,C see text).

Top:

Contribution of the largest individual scattering angle ϑ_{max} to the total scattering angle ϑ for the loop below.
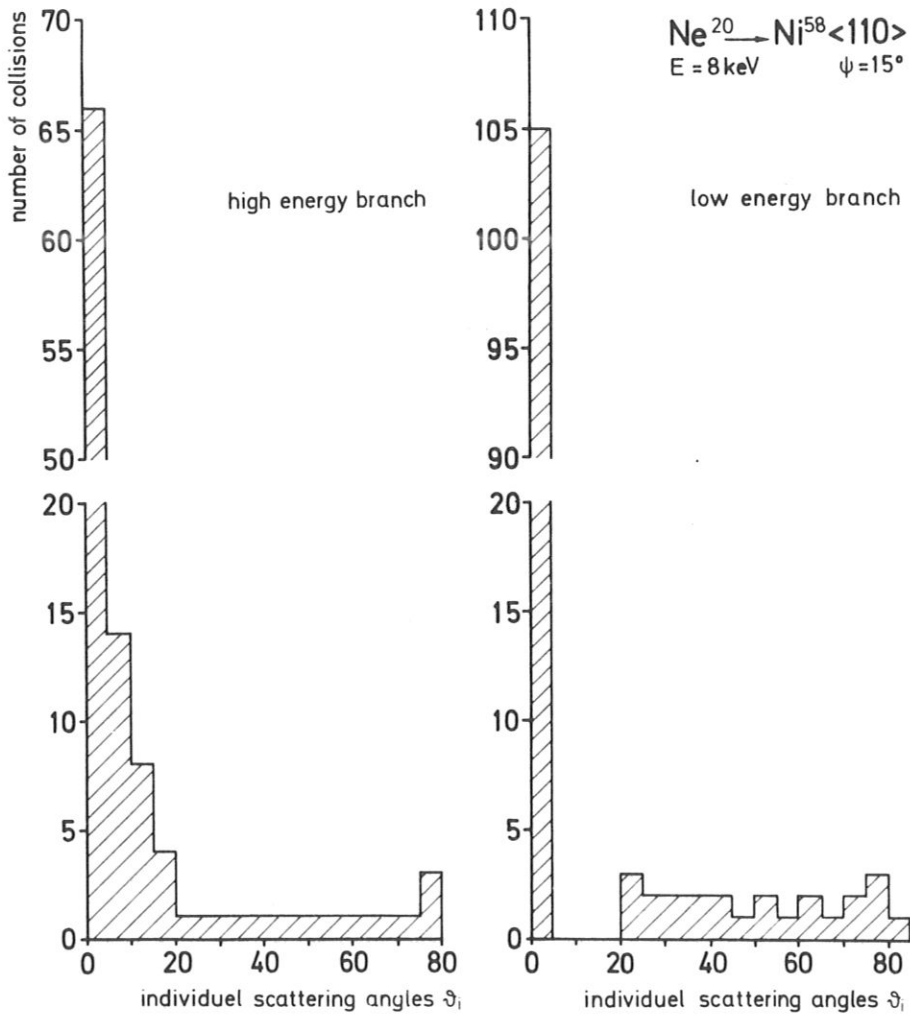
Fig. 14: Statistics of the single collision processes for the multiple scattering of Ne[+] from a ⟨110⟩ chain of Ni.
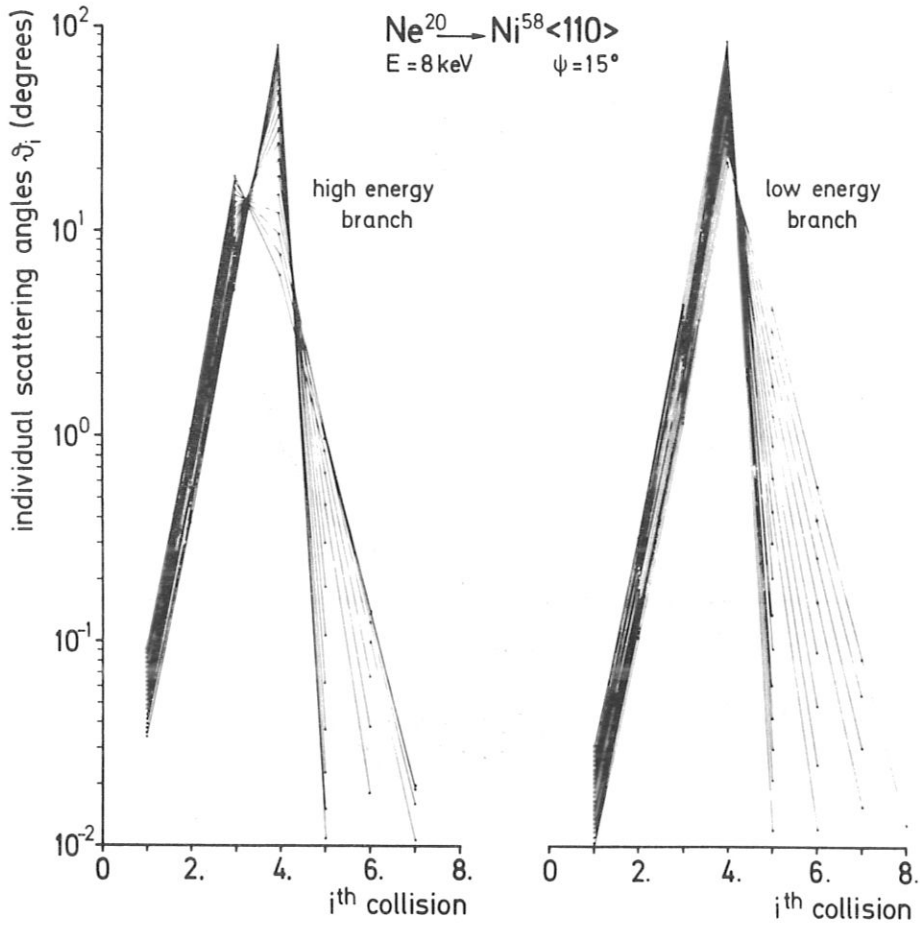
Fig. 15: Size of the individual scattering angles as a
function of collision number in multiple
scattering of Ne$^+$ from a ⟨110⟩ chain of Ni.
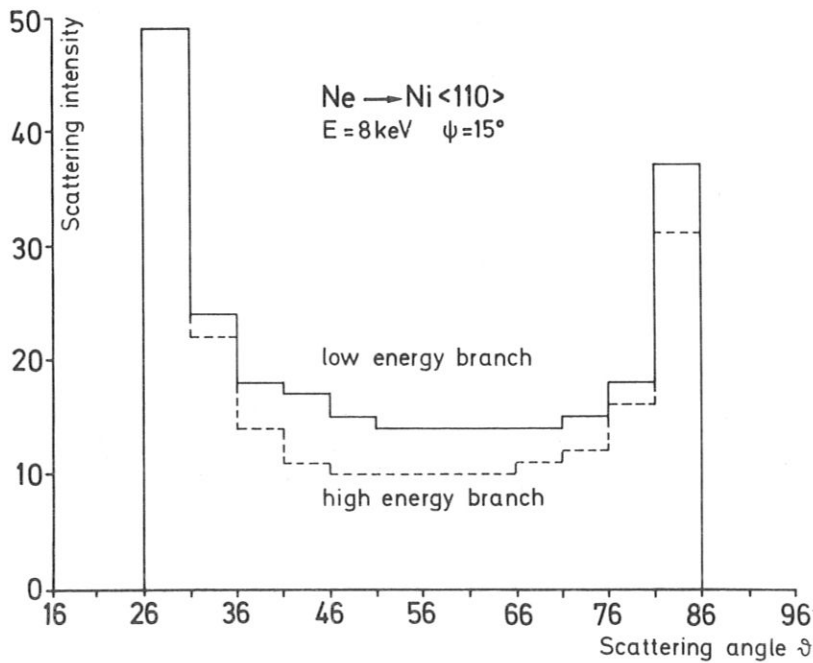
Fig. 16:

Intensity distri-
bution along the
loop.
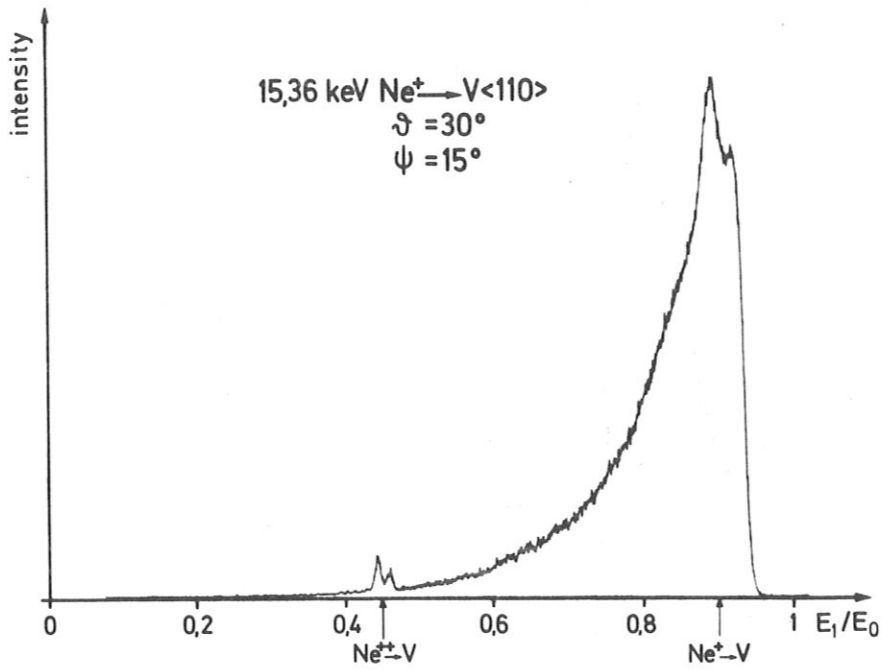
Fig. 17: Backscattering spectrum of Ne$^+$ from
a $\langle 110 \rangle$ chain of V.
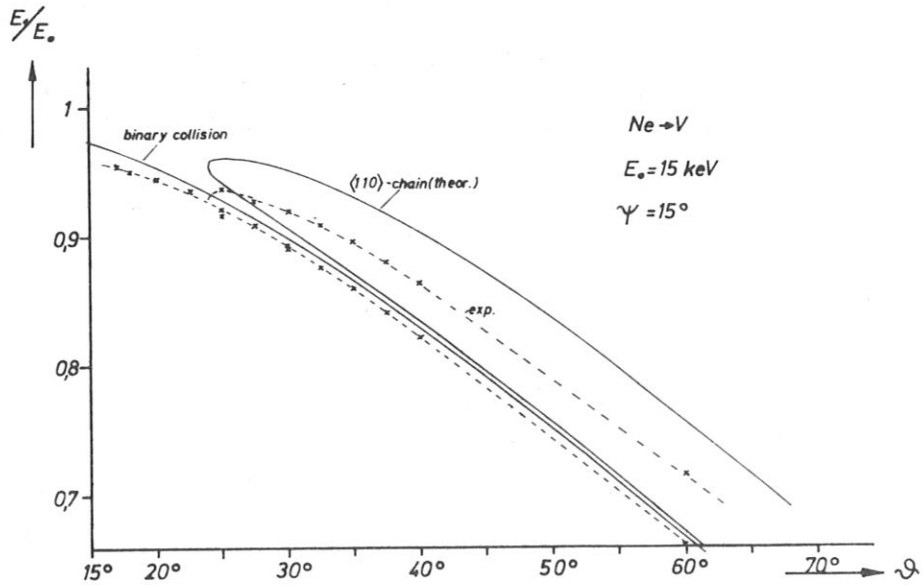
Fig. 18: Comparison of the theoretical and experimental
energies of Ne$^+$ ions with a primary energy of
15 keV scattered from a $\langle 110 \rangle$ chain of V.
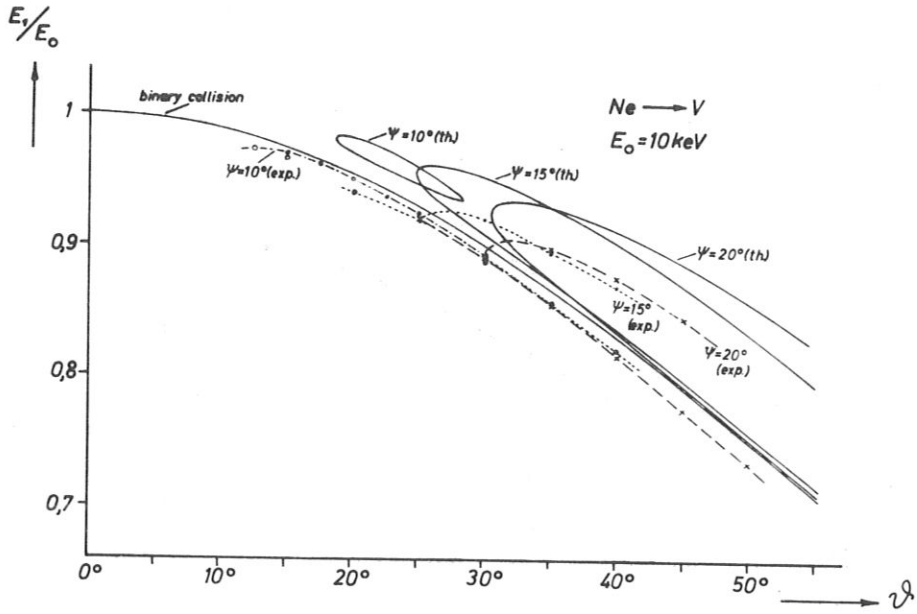
Fig. 19: like Fig. 18, but Ne⁺ with primary energy
of 10 keV.
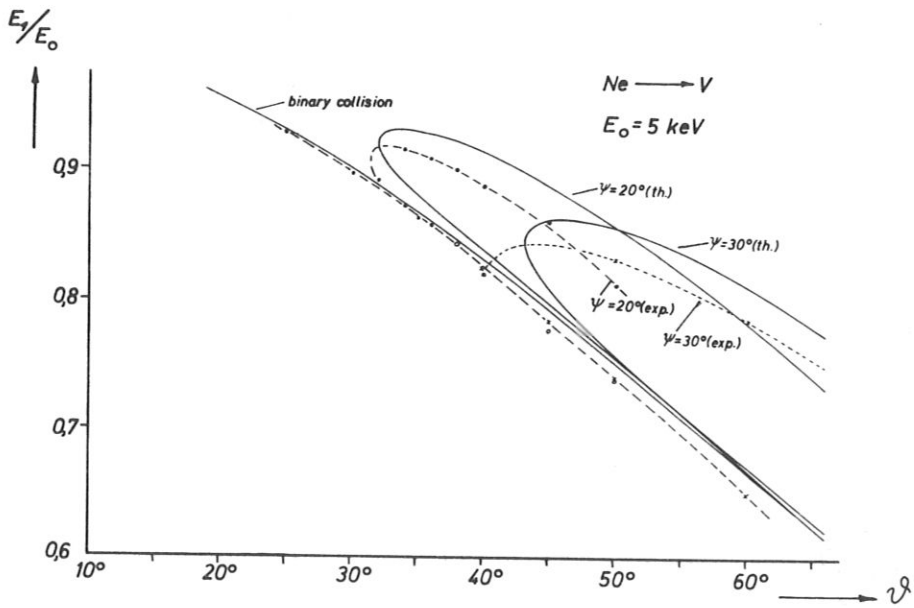
Fig. 20: like 18 and 19, but Ne⁺ with a primary
energy of 5 keV.
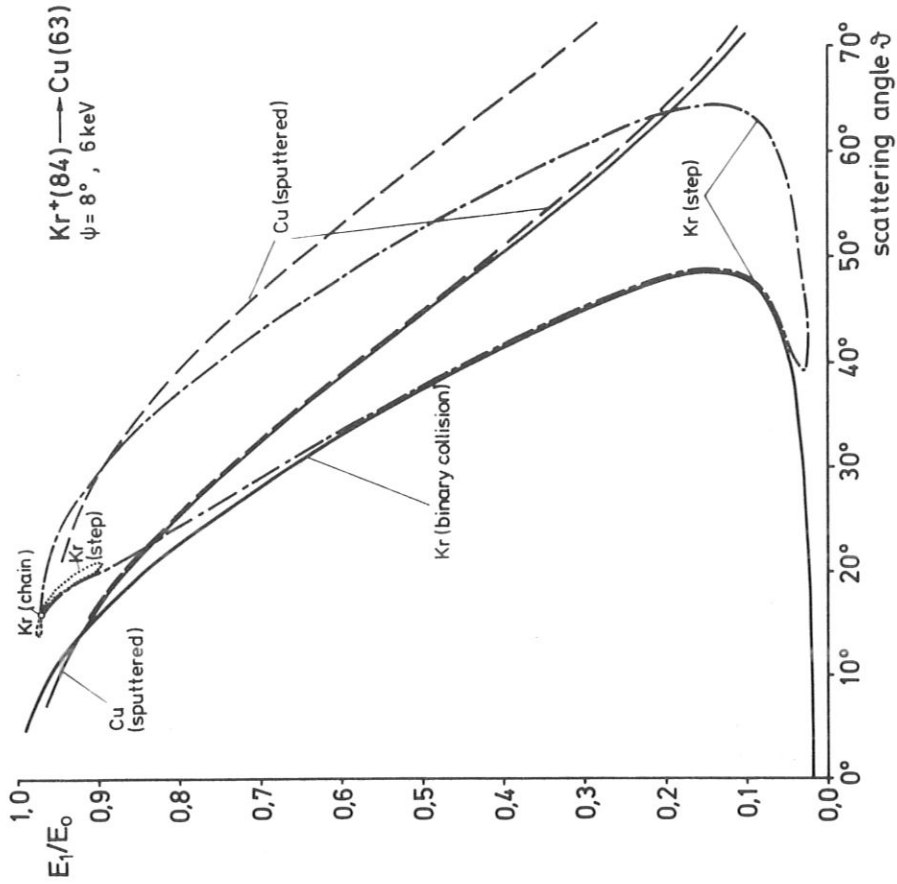
Fig. 22: Theoretical energy values of 6 keV Kr+ ions scattered from imperfect chains on copper.
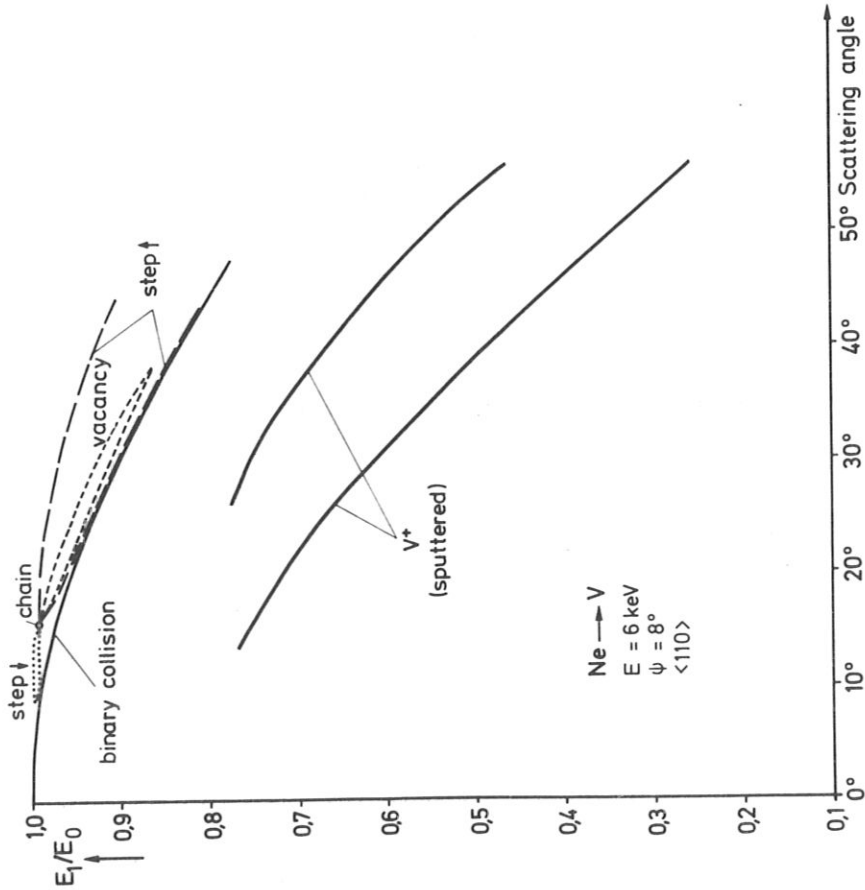
Fig. 21: Theoretical energy values of 6 keV Ne+ ions scattered from imperfect ⟨110⟩ chains of vanadium.
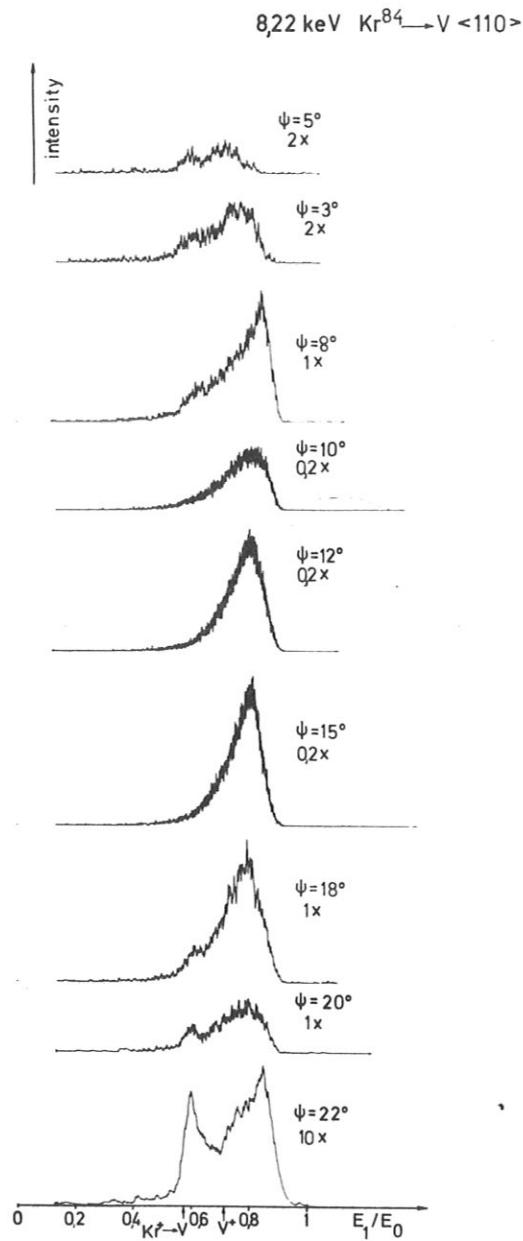
8,22 keV Kr^{84}⟶V <110>

Fig. 23: Backscattering spectra of 8.22 keV Kr^{84} ions from ⟨110⟩ chains of vanadium for a scattering angle ϑ = 30°.